

# Unidirectional spin-wave edge modes in magnonic crystal

Cite as: APL Mater. 11, 021104 (2023); doi: 10.1063/5.0134099  
Submitted: 8 November 2022 • Accepted: 16 January 2023 •  
Published Online: 13 February 2023



J. Feilhauer,<sup>1,2,a)</sup> M. Zelent,<sup>3</sup> Zhiwang Zhang,<sup>4</sup> J. Christensen,<sup>5</sup> and M. Mruczkiewicz<sup>1,2,b)</sup>

## AFFILIATIONS

<sup>1</sup>Institute of Electrical Engineering, Slovak Academy of Sciences, Dubravská Cesta 9, SK-841-04 Bratislava, Slovakia

<sup>2</sup>Centre for Advanced Materials Application CEMEA, Slovak Academy of Sciences, Dubravská Cesta 9, 845 11 Bratislava, Slovakia

<sup>3</sup>Faculty of Physics, Adam Mickiewicz University in Poznań, Umultowska 85, Poznań PL-61-614, Poland

<sup>4</sup>Department of Physics, MOE Key Laboratory of Modern Acoustics, Collaborative Innovation Center of Advanced Microstructures, Nanjing University, Nanjing 210093, China

<sup>5</sup>IMDEA Materials Institute, Calle Eric Kandel, 2, 28906 Getafe, Madrid, Spain

<sup>a)</sup>Electronic mail: [juraj.Feilhauer@savba.sk](mailto:juraj.Feilhauer@savba.sk)

<sup>b)</sup>Author to whom correspondence should be addressed: [michal.mruczkiewicz@savba.sk](mailto:michal.mruczkiewicz@savba.sk)

## ABSTRACT

We present a numerical demonstration of magnonic crystals hosting unidirectional, topologically protected edge states. The magnonic crystal is formed of dipolarly coupled Permalloy triangles. We show that due to the geometry of the block, the size of the structure can be scaled up. In addition, edge states can be found over a wide frequency range. Experimental detection of edge excitations in the considered system can be done with state-of-the-art techniques. Thus, we demonstrate a proof-of-concept magnonic Chern topological insulator nanostructure with simple geometry feasible for experimental realization. Furthermore, by tuning the strength of the perpendicular magnetic field, we induce a topological phase transition, which results in the change of direction of the topological edge state. Then, we demonstrate the magnonic switch based on this effect.

© 2023 Author(s). All article content, except where otherwise noted, is licensed under a Creative Commons Attribution (CC BY) license (<http://creativecommons.org/licenses/by/4.0/>). <https://doi.org/10.1063/5.0134099>

## I. INTRODUCTION

One of the most outstanding features of 2D topological insulators is the presence of topological edge states within the bandgap of bulk materials.<sup>1–4</sup> Protected by the time-reversal symmetry, these edge states are robust against backscattering (i.e., they are unidirectional), which makes them a very promising candidate for the information carriers in future data processing devices. Topological edge states, insensitive to defects, were demonstrated theoretically and experimentally in many wave-hosting systems, e.g., electron,<sup>5</sup> electromagnetic,<sup>6</sup> acoustic,<sup>7,8</sup> or mechanical.<sup>9</sup>

Topological magnonics is an emerging topic in modern magnetism. Until now, it mainly exploits the analogies of topological waves considered in other wave hosting systems and is mainly limited to basic theoretic model systems. However, the field of magnonics provides a platform for studying new kinds of phenomena that are specific to spin waves (SWs), due to the intrinsic nonreciprocal and nonlinear properties of SWs<sup>10,11</sup> or the reconfigurability of

magnetic states.<sup>12</sup> Therefore, the synthetic magnetic structures will play an important role in magnonics and will contribute to the development of topological waves in general.

Despite several theoretical demonstrations of topological magnons<sup>13–26</sup> or experimental proofs of a topological gap in 2D honeycomb ferromagnets,<sup>27–29</sup> the direct experimental demonstration of a magnonic unidirectional edge state is still missing. The main obstacles preventing experimental observations are the difficulty of nano-fabrication of complex geometry, low coupling between elements, difficulty controlling the magnetic state, low sensitivity of the in-plane dynamical field component, high density of modes when scaling up structures, or high damping in metallic ferromagnetic materials with Dzyaloshinskii–Moriya interaction.

A specific class of magnonic crystals (MCs) hosting the unidirectional edge states includes ferromagnetic MCs composed of dipolarly coupled nanoelements with a unit cell, magnetized in the closure domain state with fixed chirality.<sup>14,15</sup> A precursor model of this type of MC was presented in Ref. 13 as a square lattice with

the four spins in the square unit cell. These four spins are located equidistantly around the center of the unit cell, with magnetizations circulating in-plane with the given chirality. Dipolar coupling between the four spins within a single unit cell gives rise to four azimuthal SW modes with  $s$ ,  $p_x - ip_y$ ,  $p_x + ip_y$  and  $d_{x^2-y^2}$ -like symmetries. The eigen frequencies of both  $p$ -like azimuthal modes are degenerated. In the MC, the dipolar coupling of azimuthal modes from neighboring cells induces four SW bands.

By applying a perpendicular magnetic field, the spins get tilted out of the plane and the eigen frequencies of azimuthal modes are modified. The degeneracy of  $p$ -like azimuthal modes is lifted, and with increasing field, the frequency order of the four azimuthal modes can change. In the MC, this reordering of azimuthal mode frequencies can be accompanied by gap closing and successive band inversion signaling the possible topological phase transition. Indeed, as shown in Ref. 13, with increasing magnetic field, the MC exhibits several phases of topological order manifested as nonzero Chern numbers in the SW bands. As expected, in the corresponding MC with finite width, the unidirectional edge states exist in the bandgap between the topologically nontrivial bands.

Nevertheless, the extension of the four-spin model to the nano/micro-scale system is challenging and is endowed with some of the above mentioned issues, e.g., difficulty to fabricate the sample, control the magnetic state, or high density of modes when scaling up structures. Even the dipolar coupling of modes remained elusive until recent experimental demonstrations.<sup>30</sup>

Here, we present a numerical demonstration of the nanoscale realization of the topological properties shown for the four-spin model. The geometry of our MC potentially solves the experimental obstacles, and, therefore, our MC is a strong candidate for the experimental proof of the magnonic topological edge states. Moreover, we demonstrate that the properties of the edge states, such as direction of propagation, can be controlled with the strength of an external magnetic field.

## II. RESULTS

### A. Square unit cell made of Permalloy triangles

The unit cell of the considered square lattice MC is composed of a thin ferromagnetic square with two lines cut along its diagonals [see Fig. 1(a)]. Therefore, the unit cell is composed of four elementary building blocks, right-angled isosceles triangles, see Fig. 1(b). The fabrication of this type of geometry requires removing only straight lines from the ferromagnetic film, and it can be realized with MFM scratching, local anodic oxidation,<sup>31</sup> or a focused ion beam.<sup>32–34</sup> The closure domain magnetic state of the unit cell might nucleate spontaneously<sup>12</sup> or be induced with local MFM field,<sup>35,36</sup> all optical switching<sup>37</sup> or by combination of the in-plane field and variation in shape anisotropy of composing elements.<sup>38</sup> Furthermore, an efficient dipolar dynamical magnetic coupling between the elements is expected due to the large surface area of facing sides of elements and their small distance given by the thickness of the cut lines of the order of 10 nm.

The building blocks of the unit cell (we assumed Py triangles) considered in this manuscript had a thickness,  $t = 15$  nm, and the base of the triangle was set to  $a = 150$  nm, see Fig. 1(b). We assume an artificially low value of damping in spectral analysis ( $\alpha = 0.0001$ )

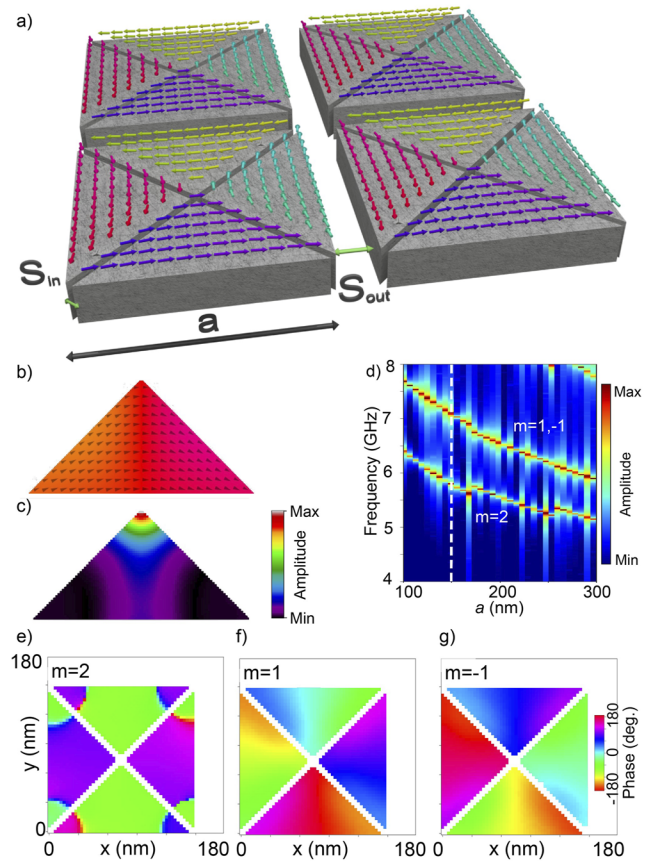


**FIG. 1.** (a) A magnonic crystal of closure domain state in a square lattice. The unit cell of a magnonic crystal is composed of a meta-square. The side length of the meta-square is  $a = 150$  nm, the thickness is  $t = 15$  nm, the inner separations between triangular elements are  $S_{in} = 6$  nm, and the outer separations between the squares are  $S_{out} = 30$  nm. (b) A right-angled isosceles triangle made of Permalloy (Py) thin film ( $t = 15$  nm). The base of the triangle is  $a = 150$  nm. The triangle is magnetized along its base in the  $+x$  direction. (c) Amplitude distribution of the dynamical component of the lowest frequency ( $f = 6.17$  GHz) eigenmode of the single Py element. (d) Frequency dependence of the azimuthal modes as a function of the size of the isolated square. (e)–(g) phase profiles of the azimuthal modes calculated at  $B_z = 50$  mT:  $m = 2$ , CCW  $m = 1$ , and CW  $m = -1$ , respectively.

and a realistic value of Py's damping in the demonstration of edge wave propagation ( $\alpha = 0.005$ ). Due to the shape anisotropy, the magnetic ground state of an isolated triangle is given by two quasi-uniform magnetic states oriented along the base of the triangle (with  $+x$  and  $-x$  orientations). We can expect that in this geometry, the lowest-frequency spin wave modes will exhibit quantizations along the magnetization direction (along the  $x$ -axis). With an increase in the triangle size, higher-order quantizations along the  $x$ -axis are expected to exhibit a lower frequency than the quasi-uniform mode, due to the specificity of dipole interactions.<sup>39</sup> However, the modes with a node in the center of the triangle (odd modes along the  $x$ -axis) will have a relatively large area of excitation within the narrower part of the triangle. These modes will be more confined, as

they are the modes that have the maximum amplitude in the center of the triangle (even modes along the  $x$ -axis). Therefore, the increase in frequencies due to confinement along the  $y$ -direction will be more pronounced for odd modes. Additionally, the magnetic state is deformed from the uniform  $\pm x$  state, and spins tend to align with the sides of the triangle. In order to satisfy the continuous rotation of spins between two sides of the triangle at the triangle apex, a spin orientation along the  $x$ -axis is formed, generating a strong local demagnetizing field. This demagnetizing field decreases the magnitude of the effective field and, correspondingly, lowers the spin precession frequency at the triangle apex.

As a result, the lowest frequency quasi-uniform triangle excitation with strong localization at the triangle apex is found at 6.17 GHz for  $a = 150$  nm, see Fig. 1(c) for the amplitude distribution. It is well below the frequency 10.15 GHz of the 1st quantized mode. Therefore, in the square formed of four Py triangles [Fig. 1(a)], we can consider the formation of four azimuthal modes from the lowest-frequency quasi-uniform excitations in triangles. These four azimuthal modes can be characterized by azimuthal quantum numbers, where mode with  $m = 0$  is a uniform SW, mode with  $m = 2$  resembles a standing wave, and modes with  $m = -1$  and  $m = 1$  correspond to the SWs traveling around the unit cell in clockwise (CW) and counterclockwise (CCW) directions, respectively. The frequencies of the three lowest azimuthal modes (with  $m = 2, 1,$  and  $-1$ ) are well separated from the frequencies of azimuthal modes formed by higher-order excitations of triangle. Phase profiles for these three azimuthal modes are plotted in Figs. 1(e)–1(g). Properties of azimuthal modes in square unit cells exhibit qualitatively the same behavior as azimuthal modes in a simple four-spin model,<sup>13</sup> assuming the coupling between the triangles within unit cells is stronger than the coupling between the triangles from neighboring unit cells. The width of the square diagonal line was set to  $S_m = 6$  nm, and the separation between the square units was much larger ( $S_{out} = 30$  nm) to satisfy this requirement.

The frequency dependence as a function of the triangle base,  $a$ , of the three lowest-frequency azimuthal modes in an isolated square unit cell is presented in Fig. 1(d). The lowest-frequency mode is  $m = 2$  [Fig. 1(e)], separated by a frequency difference  $\Delta f_{21}$  from two degenerated modes with  $m = 1$  [Fig. 1(f)] and  $m = -1$  [Fig. 1(g)]. The value of  $\Delta f_{21}$  is about 1 GHz, which is a clear manifestation of strong dynamical dipolar coupling between the triangles in a unit cell. Moreover, as Fig. 1(d) shows, this  $\Delta f_{21}$  decreases by only about 40% when  $a$  is tripled from 100 to 300 nm. This is an important result that demonstrates the possibility for scaling up the triangles' size without introducing higher-order quantization modes of the individual triangular elements, which could lead to overlapping between magnonic bands and lowering the width of the full topological gap, as discussed in the following part. In this manuscript, we limit our investigation to  $a = 150$  nm in order to demonstrate the effect and perform large-scale simulations of finite MC.

## B. Bulk band structure and bands' inversion

When creating a MC based on the unit cell described in Sec. II A, the azimuthal modes between neighboring cells are coupled, giving rise to the spin wave bands. The calculated bandstructure of infinite 2D MC is presented in Fig. 2(a), where three bands originating from three azimuthal modes with  $m = 2, 1,$  and  $-1$  are

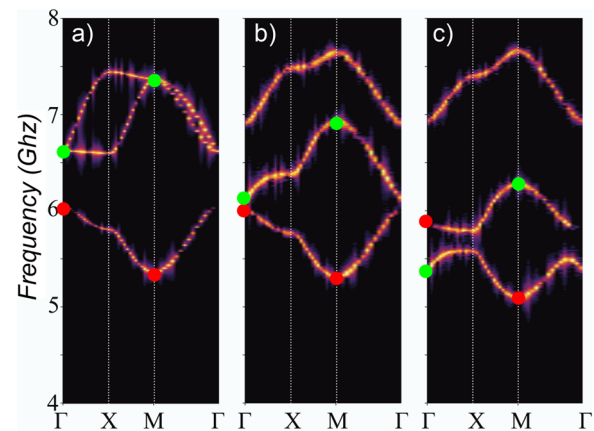


**FIG. 2.** Bandstructure of the infinite magnonic crystal at (a)  $B_z = 0$ , (b)  $B_z = 150$ , and (c)  $B_z = 330$  mT. The red and green dots indicate the Bloch waves with phase profiles equivalent to the  $m = 2$  and  $m = 1$  azimuthal modes, respectively [shown in Figs. 1(e) and 1(f)].

shown. The bandwidths (a range of frequencies within a band) of these bands are about 0.7 GHz, which confirms significant dynamical dipolar coupling between the triangles of neighboring cells. The lowest band corresponding to  $m = 2$  is separated by a gap of 0.6 GHz from the partially overlapping bands given by  $m = \pm 1$ , which is consistent with the fact that frequencies of azimuthal modes  $m = \pm 1$  are degenerated. In order to show that the two lowest bands stem from the azimuthal modes  $m = 2$  and  $1$ , we have analyzed the spatial profiles of corresponding Bloch waves at  $k = \Gamma$  and  $M$ . Red points and green points in Figs. 2(a)–2(c) mark the Bloch waves with spatial profiles the same as azimuthal modes  $m = 2$  and  $m = 1$ , respectively, depicted in Fig. 1(e) [Fig. 1(f)].

Motivated by the four-spin model, we study the evolution of the bandstructure of MC in the out-of-plane magnetic field. Particularly, we are searching for the bandgap closings, which are typical indicators of band inversions and successive topological phase transitions in periodic crystals.<sup>40</sup> Figure 2(b) shows an example of the bands in the vicinity of band closing occurring around  $B_z = 150$  mT, where bands with  $m = 2$  and  $m = 1$  almost touch at the  $\Gamma$  point. At a slightly higher magnetic field, the gap closes and reopens again [see Fig. 2(c)], but the bands are now topologically nontrivial, i.e., they are no longer constructed solely by a single azimuthal mode. Indeed, red and green points reveal that in the vicinity of  $\Gamma$  point, the dominant azimuthal modes defining the bands are inverted when compared to the topologically trivial case in Figs. 2(a) and 2(b). Now, both lowest bands are composed of a mixture of azimuthal modes  $m = 2, 1$  in a ratio depending on the position in a Brillouin zone.

To confirm the topological character of the formed bands, we perform the analysis of the infinite MC (with  $32 \times 32$  unit cells and periodic boundary conditions), extract the Bloch wavefunctions and perform numerical calculation of the Chern numbers (see Sec. IV). As expected, we found that the Chern numbers for the two lowest bands at  $B_z = 0$  T are zero, i.e., these bands are topologically trivial. However, the Chern numbers for the two lowest bands at  $B_z = 330$  mT are  $C = 1$  and  $-1$  for the lower and upper bands, respectively, which confirms their topological nature.

### C. Unidirectional edge state

In order to demonstrate the topological properties of the magnonic gap observed in Fig. 2(c), we perform calculations of the dispersion relation of the magnonic ribbon, consisting of an infinite number of square elements along the longitudinal ( $x$ ) direction and eight square elements along the transversal ( $y$ ) direction. The computational cell is set to  $32 \times 8$  with periodic boundary conditions in the  $x$ -direction, so that 32 points of the dispersion can be plotted. The results of these calculations are presented in Fig. 3(a), where the dispersion along the  $x$  axis is calculated at the bottom edge of the finite ribbon (left image) and along the center (right image). Two bands, separated by the bandgap of the width  $\sim 200$  MHz are found at the center of the structure and the unidirectional wave mode connecting the bands was found at the edge of the structure. Furthermore, we perform simulation of the same infinite ribbon at  $k = 0$  point (number of cells:  $1 \times 8$ ) with high density mesh along the  $z$ -axis (size of the computational mesh is  $c_x, c_y,$  and  $c_z = 3$  nm) to verify the influence of the non-uniform mesh along the  $z$ -axis. The intensity

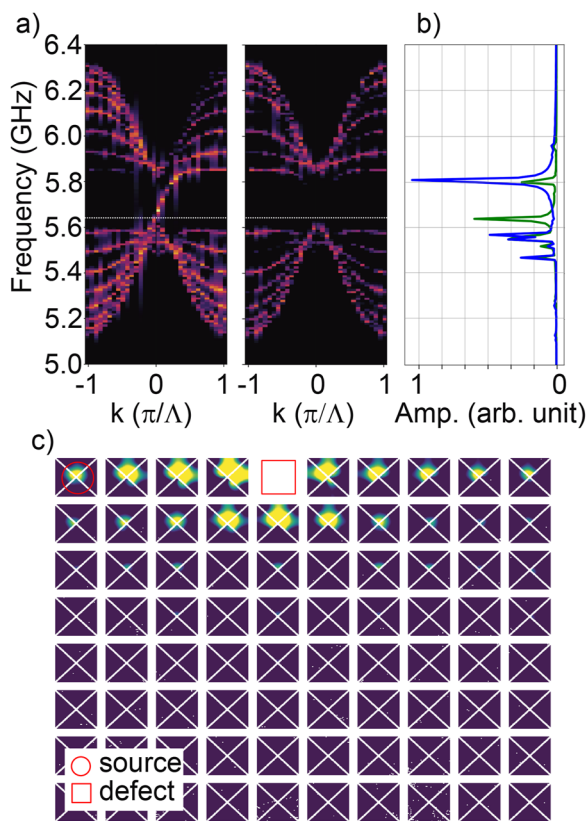


**FIG. 3.** (a) The dispersion relation at  $B_z = 330$  mT for an infinite ribbon composed of eight elements in the  $y$  direction and periodic in the  $x$  direction, calculated at the center of the stripe (left) and at the bottom edge (right). The white dotted lines indicate the frequency of the mode presented in Fig. 3(c). (b) The intensity of uniform mode,  $k = 0$ , calculated with high density mesh ( $c_x, c_y, c_z = 3$  nm) at the center (blue) and the edge (green) (c) Unidirectional wave propagation excited in a finite structure ( $10 \times 8$  elements with one defect) with sin signal applied to the left-top element at frequency,  $f = 5.65$  GHz. The propagation is calculated with the damping value  $\alpha = 0.005$ .

of the wave modes is plotted in Fig. 3(b) and shows the presence of strong edge localization at comparable frequencies.

Finally, we perform simulation of the edge state propagation in the finite structure without periodic boundary conditions ( $10 \times 8$  elements) with one defect, see Fig. 3(c). The sine signal was applied to one unit cell placed in the top right corner at frequency  $f = 5.65$  GHz, as indicated by the white dotted lines on Fig. 3(a). The intensity of the dynamical excitation is plotted after 10 ns of the maximum of the sine signal and clearly demonstrates clockwise unidirectional propagation without scattering at the defect. The realistic value of Py damping was taken into account in the simulation of edge-state propagation ( $\alpha = 0.005$ ).<sup>41</sup>

### D. Topological phases

According to the four-spin model, the gaps closing in the bandstructure of MC appear as a consequence of the frequency reordering of azimuthal modes. Namely, with an increasing magnetic field  $B_z$ , the degeneracy of the azimuthal modes  $m = \pm 1$  is lifted. The reason is the following: The unit cell in the closure domain state has a zero component of magnetization  $m_z$  at  $B_z = 0$ . As the magnetic field increases, the  $m_z$  component of magnetization is induced. The influence of  $m_z$  on the splitting of the degeneracy of azimuthal modes was explained for exchange spin waves in isolated rings in terms of the geometric Berry phase acquired by an azimuthal spin wave.<sup>42,43</sup> The same argument can be applied for the system considered here, i.e., the square composed of triangles with azimuthal modes formed by dipole interactions between triangles. As a result, the frequency of azimuthal mode  $m = 1$  decreases with increasing  $B_z$  in contrast to the frequency of  $m = -1$ , which increases. Moreover, with increasing  $B_z$ , the frequencies of the two lowest azimuthal modes, with  $m = 1$  and  $m = 2$ , approach each other and eventually overlap, which leads to hybridization and gap closing between corresponding bands in MC. In the four-spin model, when increasing  $B_z$ , the first such gap closing appears at the  $\Gamma$  point and then the closings at the X and M points follow. Each of these gap closings is associated with a change in the topological phase of MC.

In the case of our MC, the azimuthal modes and bands show qualitatively similar behavior as described by the four-spin model. To extend the analysis of the bandstructure evolution in magnetic field, we show in Figs. 4(a)–4(c) the frequencies of magnonic bands at specific points  $k = \Gamma, K,$  and  $M$  respectively. As the magnetic field increases in the range from 0 to 300 mT, the frequencies of the bands formed by  $m = 1$  and  $m = -1$  azimuthal modes decrease and increase, respectively, i.e., the gap between those bands expands. The magnetic field in the considered range has a relatively low influence on the band formed by the  $m = 2$  azimuthal mode. As a result, at  $B_z = 200$  mT, the two lowest bands touch at the  $\Gamma$  point [see Fig. 4(a)], and the magnonic crystal undergoes a topological phase transition into a topologically non-trivial state. With further increase in magnetic field, the magnonic gap between the two lowest bands reopens, and the bands become inverted in the vicinity of  $\Gamma$  point, as discussed in section B.

Elevating the magnetic field above 300 mT, the frequencies of all bands steeply decrease. Figure 4(b) shows that at  $B_z = 430$  mT, there is another gap closing between the two lowest bands at the X point, signaling a topological phase transition. Here, the Chern numbers of the two lowest bands are reversed, i.e., from  $C = 1$

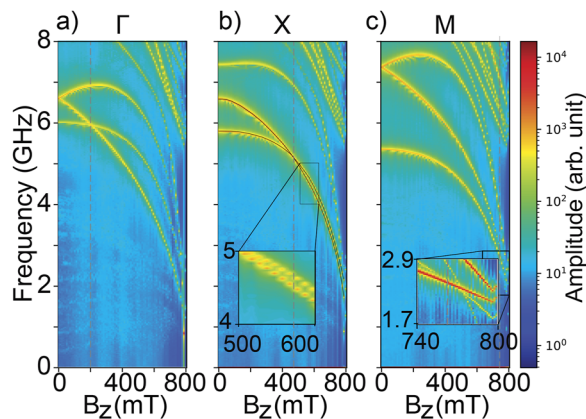


**FIG. 4.** Band frequencies at (a)  $k = \Gamma$ , (b)  $k = X$ , and (c)  $k = M$  points as a function of the out-of-plane magnetic field  $B_z$ . Dashed lines indicate the gap closing between the two lowest bands. Insets show the zoomed regions.

(lowest band) and  $-1$  (2nd lowest band) in the range  $200 < B_z < 430$  mT to  $C = -1$  and  $1$ . This reversal of Chern numbers has direct consequence on the direction of topological edge states in finite MCs, as discussed in detail in Sec. II E. When increasing the magnetic field even more, the gap of about 150 MHz between the two lowest bands reopens again, which is visible in the inset of Fig. 4(b).

Further increase of the field to  $B_z = 760$  mT shows the crossing of the  $m = 2$  and  $m = 1$  bands at the  $k = M$  point, and it is followed by a change of magnetic order at  $B_z = 782$  mT (from a chiral state with a nonzero out of plane component to a state magnetized fully out of plane). Within the region between  $B_z = 760$  mT and  $B_z = 782$  mT, we observe complex band structures due to multi-mode overlapping [see inset in Fig. 4(c)].

Qualitatively, the same results and order of topological phases were predicted in the four-spin model in Ref. 13. The tight binding model presented there explains the main features of the dipole interaction that lead to the presence of the topological phases and inversion of the Chern numbers at the  $k = X$  point for the considered MC.

### E. Magnonic switch

Furthermore, we present the band dispersions of two ribbons with a straight edge and a zigzag edge [Figs. 5(a) and 5(e) respectively], calculated at the bottom edge of the ribbons, at different magnetic fields in the range from 330 to 530 mT. These magnetic field ranges cover the transition between two topological phases occurring at 430 mT. Figures 5(b) and 5(f) show that the clockwise propagating edge state with positive group velocity  $\propto df/dk$  is present in the gap at  $B_z = 330$  mT. With an increase in the magnetic field toward the transition at  $B_z = 430$  mT, the magnonic gap width is decreasing [see Figs. 5(c) and 5(g)]. After the transition, at higher fields  $B_z = 530$  mT [Figs. 5(d) and 5(h)], the edge state is observed in the gap with the opposite propagation direction (negative group velocity) as compared to the field at  $B_z = 330$  mT. The change of edge state propagation direction is triggered by

the change of the topological phase, accompanied by the reversal of the Chern numbers after the crossing of bands at the  $k = X$  point [Fig. 4(b)].

Finally, based on the change of topological phase induced by a magnetic field, we demonstrate the effect of a magnonic switch: a magnonic element that transfers the information in the direction determined by the value of the magnetic field and frequency of excitation. We performed the simulations of finite structure with the zigzag edge and plot the signal transmitted at time frame 10 ns after the maximum of the sin impulse for two magnetic fields  $B_z = 330$  mT [see Fig. 6(a)] and  $B_z = 530$  mT [see Fig. 6(b)]. The excitation frequencies were 5.91 and 4.96 GHz, respectively. As expected, the direction of the edge state is reversed at  $B_z = 530$  mT as compared to the direction of propagation at the field  $B_z = 330$  mT. The control of topological state direction creates a base for the development of reprogrammable, immune to back-scattering magnonic applications, e.g., highly efficient magnonic diodes.

### III. SUMMARY

We have numerically demonstrated a topological magnonic crystal (MC) hosting unidirectional edge states that has potential for experimental realization. The MC proposed in this manuscript is a nanoscopic extension of the four-spin model,<sup>13</sup> and it simultaneously addresses most of the issues (e.g., complex geometry, weak coupling between the elements, high density of modes leading to a small magnonic gap, . . .) preventing experimental demonstration of the topological edge states.

Namely, the geometry of our MC is very simple—it can be created by removing narrow straight lines from the thin Permalloy film. The unit cell of the MC consists of four isosceles right-angle triangles magnetized along their bases. Static magnetic moments of triangles circulate around the center of the unit cell with fixed chirality. The lowest-frequency spin wave eigenexcitation of a single triangle is well separated from the higher modes, and its amplitude is localized at the triangle apex. Therefore, the excitations of four triangles within a unit cell are strongly dipolarly coupled, creating four azimuthal modes with significant frequency differences. Dipolar coupling between the azimuthal modes from neighboring cells gives rise to four magnonic bands in the corresponding MC, separated by a wide gap of about several hundreds of MHz.

The optimization of the structure dimensions for an experimental realization of topological MC with nanoetching techniques is needed. This task should take into account the reduction of inter-cell dipolar coupling with scaling up of the structure dimensions, e.g., an increase in the lattice constant or separation between elements. However, this effect can be compensated by an increase in the structure thickness.

We have shown that by increasing the perpendicular magnetic field, the MC undergoes a couple of topological phase transitions, and the unidirectional edge states can be excited within the bulk bandgap in the MC with a finite width. Moreover, by tuning the magnetic field and the excitation frequency, the propagation direction of the edge state can be reversed, which could be utilized in a magnonic switch. We consider that this property will allow for

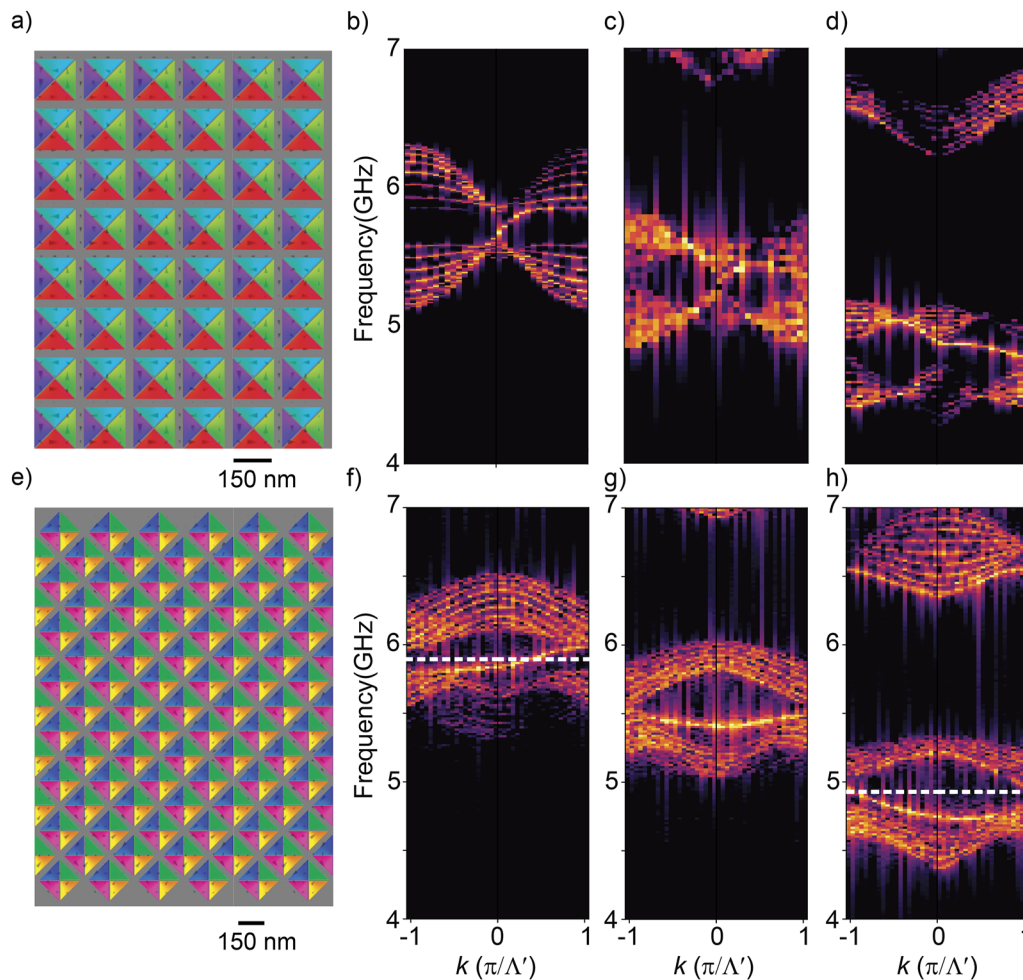


**FIG. 5.** (a) A straight-edge magnonic stripe consisting of eight elements along the  $y$  axis and an infinite number of elements along the  $x$  axis. (b)–(d) Dispersion relations of a straight-edge magnonic stripe at magnetic fields:  $B_z = 330$  mT,  $B_z = 430$  mT, and  $B_z = 530$  mT, respectively, calculated at the bottom edge of the stripe. (e) A zigzag-edge magnonic stripe consisting of eight elements along the  $y$  axis and an infinite number of elements along the  $x$  axis. (f)–(h) Dispersion relations of a zigzag-edge magnonic stripe at magnetic fields:  $B_z = 330$  mT,  $B_z = 430$  mT, and  $B_z = 530$  mT, respectively, calculated at the bottom edge of the stripe.

designs of reprogrammable magnonic elements based on robust topological waves.

#### IV. SUPPORTING INFORMATION

##### A. Parameters

Throughout the present paper, in the numerical simulations, we use the following values of material parameters: saturation magnetization  $M_s = 0.8 \times 10^6$  A/m, exchange stiffness constant  $A = 1.3 \times 10^{-11}$  J/m. The Gilbert damping parameter used in the dynamical simulations was  $\alpha = 0.0001$  for the calculation of mode frequencies and dispersion relations and  $\alpha = 0.005$  for the confirmation of unidirectional edge propagation within the gap. This set of parameter values corresponds to Py films. The mesh size was set to

$c_x = c_y = 3$  nm and  $c_z = 15$  nm for most of the simulations, with the exception of the high mesh density simulation, where the mesh was set to  $c_x = c_y = c_z = 3$  nm.

##### B. Model

We investigate the spectrum of spin excitations by performing finite difference time domain (FDTD) micromagnetic simulations using mumax<sup>3,44</sup>. The calculations are based on the Landau–Lifshitz (LL) equation describing the dynamics of reduced magnetization  $\mathbf{m}$  given by

$$\frac{\partial \mathbf{m}(\mathbf{r}, t)}{\partial t} = \boldsymbol{\tau}, \quad (1)$$

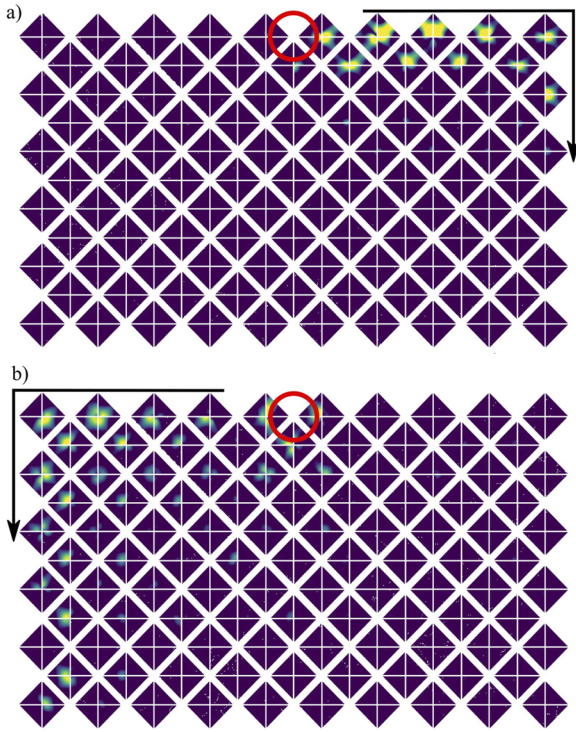


**FIG. 6.** Snapshot at time 10 ns after the maximum value of the applied sine impulse applied locally (red circle) for (a)  $B_z = 330$  mT and  $f = 5.91$  GHz and (b)  $B_z = 530$  mT and  $f = 4.96$  GHz.

where  $\tau$  is the torque, which can be expressed as

$$\tau = |\gamma| \frac{1}{1 + \alpha^2} (\mathbf{m} \times \mathbf{B}_{\text{eff}} + \alpha (\mathbf{m} \times (\mathbf{m} \times \mathbf{B}_{\text{eff}}))). \quad (2)$$

Here,  $\gamma$  is the gyromagnetic ratio,  $\alpha$  is a dimensionless damping parameter, and  $\mathbf{B}_{\text{eff}}$  is the effective magnetic field, which is the sum of the external magnetic field  $\mathbf{B}_{\text{ext}}$ , the magnetostatic field  $\mathbf{B}_{\text{m}}$ , the isotropic Heisenberg exchange field  $\mathbf{B}_{\text{ex}}$  (proportional to the exchange stiffness constant  $A$ ),

$$\mathbf{B}_{\text{eff}} = \mathbf{B}_{\text{ext}} + \mathbf{B}_{\text{m}} + \mathbf{B}_{\text{ex}}. \quad (3)$$

### C. Spin wave excitation

Our simulations were performed as follows: An approximate closure domain state was assumed as the initial magnetization configuration in the unit cell, which was then relaxed to the minimum energy state. The stable magnetization configurations were excited by a low-amplitude variable magnetic field  $(b_x, b_y, b_z)$ , the time dependence of which is represented by the continuous function

$$b_{x,y,z}(x, y, t) = RN_{x,y,z}(x, y) I \text{sinc}(2\pi f_{\text{max}}(t - t_0)), \quad (4)$$

with the cut-off frequency  $f_{\text{max}} = 12.5$  GHz and  $t_0 = 1$  ns. The modulation amplitude of the sinc signal was  $I = 0.5$  mT. For efficient excitation and detection of the azimuthal modes, a random spatial

modulation,  $RN(x, y)$ , of the external magnetic field was introduced in each cell. The RN is characterized by a normal distribution centered at 0 with a standard deviation equal to 1.

In order to confirm the unidirectional propagation of the edge mode, the sin signal was applied locally in the longitudinal direction, i.e., it has the form of  $[b_x(t), 0, 0]$  with

$$b_x(t) = \begin{cases} \frac{t}{t_0} I_{\text{sin}} \sin(2\pi f t), & 0 < t < t_0 \\ \left(-\frac{t}{t_0} I_{\text{sin}} + 2I_{\text{sin}}\right) \sin(2\pi f t), & t_0 < t < 2t_0 \\ 0, & 2t_0 < t \end{cases} \quad (5)$$

where  $I_{\text{sin}} = 0.05$  mT,  $t_0 = 10$  ns, and  $f$  is the excited frequency.

### D. Dynamical evaluation

In order to evaluate the spectral properties of periodic structures, we follow the procedure described in Ref. 45. We applied a multidimensional Fourier transform to the dynamical signal of magnetization components  $\delta m_{x,y,z}(x, y, t)$ , i.e.,  $FT_{\beta}(f, k_x, k_y) = FFTN(\delta m_{\beta}(x, y, t))$  with  $\beta = x, y, z$ . By summing the squares of magnitudes of functions  $FT_{\beta}$ , we receive the power spectral density function,  $P(f, k_x, k_y)$ , that is periodic in  $k$ -space with periodicity defined by the reciprocal lattice vector  $G = (\frac{2\pi}{\Lambda}, \frac{2\pi}{\Lambda})$ , where  $\Lambda = a + S_{\text{out}}$  is a period of MC. For each point  $(k_x, k_y)$  in the Brillouin zone, we identify the peaks in  $P(f, k_x, k_y)$ , which yield the frequencies  $f_n(k_x, k_y)$  of individual spin wave bands numbered by  $n$ .

In order to evaluate the spectral properties of ribbons (i.e., structures periodic along the  $x$  direction and finite along the  $y$  direction), we performed the Fourier transform of  $\delta m_{x,y,z}(x, y, t)$  in the  $x$  direction and time and obtained  $FT_{\beta}(y, f, k_x)$ . The summation of the squared magnitudes of  $FT_{\beta}$  over  $\beta$  yielded the ribbon power spectral density  $P(y, f, k_x)$ . The maxima of  $P$  define the ribbon local bandstructure  $f_n(y, k_x)$  at different transversal positions  $y$ , as shown in Figs. 3 and 5.

### E. Chern number

To explore the topological properties of spin wave bands, the usual procedure is to translate the undamped ( $\alpha = 0$ ) spin wave dynamics driven by LL Eq. (1) into a formalism analogous to the quantum systems driven by the Schrödinger equation.<sup>15,14,46</sup> Then, the Bloch formalism and standard procedures for the calculation of topological invariants can be applied. At first, the LL equation is linearized, considering that the dynamical part of the magnetization,  $\delta \mathbf{m}(\mathbf{r})$ , is small in comparison to the static part,  $\mathbf{m}_0(\mathbf{r})$ . Then, the magnetization at each position  $\mathbf{r}_j$  is written on a basis where  $\mathbf{m}_0(\mathbf{r}_j)$  is oriented along the  $z$ -axis and  $\delta \mathbf{m}(\mathbf{r}_j)$  lies in an  $xy$ -plane, i.e.,  $\delta \mathbf{m}(\mathbf{r}_j) = (\delta s_x(\mathbf{r}_j), \delta s_y(\mathbf{r}_j), 0)$ .

Assuming the spin excitations in a periodic magnonic crystal, the Bloch theorem can be applied, i.e.,  $\delta s_x(\mathbf{r}_j) = X_{\mathbf{k}}(\mathbf{r}_j) e^{i\mathbf{k} \cdot \mathbf{r}_j}$  and  $\delta s_y(\mathbf{r}_j) = Y_{\mathbf{k}}(\mathbf{r}_j) e^{i\mathbf{k} \cdot \mathbf{r}_j}$ , where  $X_{\mathbf{k}}(\mathbf{r}_j)$  and  $Y_{\mathbf{k}}(\mathbf{r}_j)$  are time-dependent and periodic with the periodicity of the magnonic crystal.

Next, the magnonic creation  $m_+(\mathbf{r}_j) = X_{\mathbf{k}}(\mathbf{r}_j) + iY_{\mathbf{k}}(\mathbf{r}_j)$  and annihilation  $m_-(\mathbf{r}_j) = X_{\mathbf{k}}(\mathbf{r}_j) - iY_{\mathbf{k}}(\mathbf{r}_j)$  fields are introduced, which

enables to rewrite the linearized LL equation for magnonic crystal in a Schrödinger-like form,

$$i \frac{\partial \psi(\mathbf{k})}{\partial t} = \eta H \psi(\mathbf{k}), \quad (6)$$

where  $H$  is Hermitian and  $\eta$  is a matrix with only diagonal elements being  $1, -1, 1, -1, \dots$

Vector  $\psi(\mathbf{k}) = (m_+(\mathbf{r}_1), m_-(\mathbf{r}_1), m_+(\mathbf{r}_2), m_-(\mathbf{r}_2), \dots)^T$  has  $2N$  elements, with  $N$  being the number of coupled spins in a unit cell of magnonic crystal. When assuming  $\psi(\mathbf{k}) = \varphi(\mathbf{k})e^{-i\omega t}$ , the stationary solutions of (6) obey the equation

$$\omega(\mathbf{k})\varphi(\mathbf{k}) = \eta H \varphi(\mathbf{k}). \quad (7)$$

In general, the Chern number of the  $n$ -th band is defined as

$$c_n = \frac{1}{2\pi i} \int F_{12}(\mathbf{k}) d\mathbf{k}, \quad (8)$$

where the integral runs over the whole Brillouin zone and  $F_{12}(\mathbf{k})$  is a Berry curvature defined as

$$F_{12}(\mathbf{k}) = \partial_1 A_2(\mathbf{k}) - \partial_2 A_1(\mathbf{k}) \quad (9)$$

with  $A_\mu(\mathbf{k})$  being the Berry connection,

$$A_\mu(\mathbf{k}) = \frac{\langle n(\mathbf{k}) | \partial_\mu | n(\mathbf{k}) \rangle}{|\langle n(\mathbf{k}) | n(\mathbf{k}) \rangle|}. \quad (10)$$

In the case of spin wave eigenstates  $\varphi(\mathbf{k})$  obeying Eq. (7), the scalar product in (10) reads

$$\langle n(\mathbf{k}) | n(\mathbf{k}) \rangle = \varphi^\dagger(\mathbf{k}) \eta \varphi(\mathbf{k}). \quad (11)$$

The expression for Berry connection (10) is, however, gauge-dependent, and, in practice, this formula can be used only in the case when the analytical form of eigenstates  $\varphi$  with a fixed gauge is known. In our case, we obtain the eigenstates  $\varphi(\mathbf{k})$  numerically from the micromagnetic simulation (see the paragraph below), and the complex phase of each eigenstate is arbitrary. In addition, the eigenstates  $\varphi(\mathbf{k})$  are evaluated at discrete points across the Brillouin zone; therefore, the integral in (8) is replaced with the sum,

$$c_n = \frac{1}{2\pi i} \sum F_{12}(\mathbf{k}) \Delta \mathbf{k}_1 \Delta \mathbf{k}_2, \quad (12)$$

where the summands can be expressed in a gauge invariant form<sup>47,48</sup>

$$F_{12}(\mathbf{k}) \Delta \mathbf{k}_1 \Delta \mathbf{k}_2 = \ln \left[ \frac{U_1(\mathbf{k}) U_2(\mathbf{k} + \Delta \mathbf{k}_1)}{U_1(\mathbf{k} + \Delta \mathbf{k}_2) U_2(\mathbf{k})} \right] \quad (13)$$

with

$$U_\mu(\mathbf{k}) = \frac{\langle n(\mathbf{k}) | n(\mathbf{k} + \Delta \mathbf{k}_\mu) \rangle}{|\langle n(\mathbf{k}) | n(\mathbf{k} + \Delta \mathbf{k}_\mu) \rangle|}. \quad (14)$$

In order to obtain the Bloch wave-functions of the spin wave bands from our micromagnetic calculations, we extract the values of Fourier transforms  $FT_\beta(f_{n,k_x,k_y}, k_x + \frac{r2\pi}{\Lambda}, k_y + \frac{s2\pi}{\Lambda})$ , where  $r, s$  are integers and set 0 for other values of  $FT_\beta(f, k_x, k_y)$  functions. Finally, we performed the inverse Fourier transformation to obtain the Bloch wave function  $\delta \mathbf{m}'_{n,k_x,k_y}(x, y)$  of the  $n$ -th band at  $k = (k_x, k_y)$ . Functions  $\delta \mathbf{m}'_{n,k_x,k_y}(x, y)$  can be readily transformed into the form of  $\varphi(\mathbf{k})$ , and the Chern number (12) of the  $n$ -th band can be calculated.

## ACKNOWLEDGMENTS

The research has received funding from the Slovak Grant Agency APVV (Grant No. APVV-19-0311 (RSWFA)) and the VEGA agency (Grant No. VEGA-2/0177/21). This study was performed during the implementation of the project Building-up Center for advanced materials application of the Slovak Academy of Sciences, ITMS project code 313021T081 supported by Research and Innovation Operational Program funded by the ERDF (50%). The research has received funding from the National Science Center of Poland, Grant No. UMO-2018/30/Q/ST3/00416. The simulations were partially performed at the Poznan Supercomputing and Networking Center (Grant No. 398).

## AUTHOR DECLARATIONS

### Conflict of Interest

The authors have no conflicts to disclose.

## Author Contributions

**J. Feilhauer:** Conceptualization (equal); Data curation (equal); Formal analysis (equal); Funding acquisition (equal); Investigation (equal); Methodology (equal); Project administration (equal); Resources (equal); Software (equal); Supervision (equal); Validation (equal); Visualization (equal); Writing – original draft (equal); Writing – review & editing (equal). **M. Zelen:** Conceptualization (equal); Formal analysis (equal); Investigation (equal); Methodology (equal); Software (equal); Supervision (equal); Validation (equal); Visualization (equal); Writing – original draft (equal); Writing – review & editing (equal). **Zhiwang Zhang:** Conceptualization (equal); Formal analysis (equal); Investigation (equal); Methodology (equal); Software (equal); Validation (equal); Visualization (equal); Writing – review & editing (equal). **J. Christensen:** Conceptualization (equal); Formal analysis (equal); Investigation (equal); Supervision (equal); Validation (equal); Writing – review & editing (equal). **M. Mruczkiewicz:** Conceptualization (equal); Data curation (equal); Formal analysis (equal); Funding acquisition (equal); Investigation (equal); Methodology (equal); Project administration (equal); Resources (equal); Software (equal); Supervision (equal); Validation (equal); Visualization (equal); Writing – original draft (equal); Writing – review & editing (equal).

## DATA AVAILABILITY

The data that support the findings of this study are available from the corresponding author upon reasonable request.

## REFERENCES

- 1 K. Von Klitzing, *Rev. Mod. Phys.* **58**, 519 (1986).
- 2 D. J. Thouless, M. Kohmoto, M. P. Nightingale, and M. den Nijs, *Phys. Rev. Lett.* **49**, 405 (1982).
- 3 M. V. Berry, *Proc. R. Soc. London, Ser. A* **392**, 45 (1984).
- 4 F. D. M. Haldane, *Phys. Rev. Lett.* **61**, 2015 (1988).
- 5 X.-B. Li, W.-K. Huang, Y.-Y. Lv, K.-W. Zhang, C.-L. Yang, B.-B. Zhang, Y. B. Chen, S.-H. Yao, J. Zhou, M.-H. Lu *et al.*, *Phys. Rev. Lett.* **116**, 176803 (2016).
- 6 M. Hafezi, S. Mittal, J. Fan, A. Migdall, and J. M. Taylor, *Nat. Photonics* **7**, 1001 (2013).

- <sup>7</sup>C. He, X. Ni, H. Ge, X.-C. Sun, Y.-B. Chen, M.-H. Lu, X.-P. Liu, and Y.-F. Chen, *Nat. Phys.* **12**, 1124 (2016).
- <sup>8</sup>X. Zhang, M. Xiao, Y. Cheng, M.-H. Lu, and J. Christensen, *Commun. Phys.* **1**, 1 (2018).
- <sup>9</sup>L. M. Nash, D. Kleckner, A. Read, V. Vitelli, A. M. Turner, and W. T. M. Irvine, *Proc. Natl. Acad. Sci. U. S. A.* **112**, 14495 (2015).
- <sup>10</sup>S. R. Seshadri, *Proc. IEEE* **58**, 506 (1970).
- <sup>11</sup>A. Mahmoud, F. Ciubotaru, F. Vanderveken, A. V. Chumak, S. Hamdioui, C. Adelman, and S. Cotozana, *J. Appl. Phys.* **128**, 161101 (2020).
- <sup>12</sup>J. Lehmann, A. Bortis, P. M. Derlet, C. Donnelly, N. Leo, L. J. Heyderman, and M. Fiebig, *Nat. Nanotechnol.* **15**, 896 (2020).
- <sup>13</sup>R. Shindou, J.-i. Ohe, R. Matsumoto, S. Murakami, and E. Saitoh, *Phys. Rev. B* **87**, 174402 (2013).
- <sup>14</sup>R. Shindou, R. Matsumoto, S. Murakami, and J.-i. Ohe, *Phys. Rev. B* **87**, 174427 (2013).
- <sup>15</sup>R. Shindou and J.-i. Ohe, *Phys. Rev. B* **89**, 054412 (2014).
- <sup>16</sup>A. Mook, J. Henk, and I. Mertig, *Phys. Rev. B* **90**, 024412 (2014).
- <sup>17</sup>A. Roldán-Molina, A. S. Nunez, and J. Fernández-Rossier, *New J. Phys.* **18**, 045015 (2016).
- <sup>18</sup>X. Wang, Y. Su, and X. Wang, *Phys. Rev. B* **95**, 014435 (2017).
- <sup>19</sup>S. K. Kim and Y. Tserkovnyak, *Phys. Rev. Lett.* **119**, 077204 (2017).
- <sup>20</sup>Z.-X. Li, C. Wang, Y. Cao, and P. Yan, *Phys. Rev. B* **98**, 180407 (2018).
- <sup>21</sup>Y.-M. Li, J. Xiao, and K. Chang, *Nano Lett.* **18**, 3032 (2018).
- <sup>22</sup>Z. Li, Y. Cao, P. Yan, and X. Wang, *npj Comput. Mater.* **5**, 107 (2019).
- <sup>23</sup>S. A. Díaz, J. Klinovaja, and D. Loss, *Phys. Rev. Lett.* **122**, 187203 (2019).
- <sup>24</sup>S. A. Díaz, T. Hirokawa, J. Klinovaja, and D. Loss, *Phys. Rev. Res.* **2**, 013231 (2020).
- <sup>25</sup>J. Chen, H. Yu, and G. Gubbiotti, *J. Phys. D: Appl. Phys.* **55**, 123001 (2021).
- <sup>26</sup>A. Corticelli, R. Moessner, and P. McClarty, *Phys. Rev. B* **105**, 064430 (2022).
- <sup>27</sup>R. Chisnell, J. S. Helton, D. E. Freedman, D. K. Singh, R. I. Bewley, D. G. Nocera, and Y. S. Lee, *Phys. Rev. Lett.* **115**, 147201 (2015).
- <sup>28</sup>L. Chen, J.-H. Chung, B. Gao, T. Chen, M. B. Stone, A. I. Kolesnikov, Q. Huang, and P. Dai, *Phys. Rev. X* **8**, 041028 (2018).
- <sup>29</sup>Z. Cai, S. Bao, Z.-L. Gu, Y.-P. Gao, Z. Ma, Y. Shangguan, W. Si, Z.-Y. Dong, W. Wang, Y. Wu *et al.*, *Phys. Rev. B* **104**, L020402 (2021).
- <sup>30</sup>T. Dion, J. C. Gartside, A. Vanstone, K. D. Stenning, D. M. Arroo, H. Kurebayashi, and W. R. Branford, *Phys. Rev. Res.* **4**, 013107 (2022).
- <sup>31</sup>K. Watanabe, Y. Takemura, Y. Shimazu, and J. Shirakashi, *Nanotechnology* **15**, S566 (2004).
- <sup>32</sup>O. Scholder, K. Jefimovs, I. Shorubalko, C. Hafner, U. Sennhauser, and G.-L. Bona, *Nanotechnology* **24**, 395301 (2013).
- <sup>33</sup>M. Melli, A. Polyakov, D. Gargas, C. Huynh, L. Scipioni, W. Bao, D. F. Ogletree, P. J. Schuck, S. Cabrini, and A. Weber-Bargioni, *Nano Lett.* **13**, 2687 (2013).
- <sup>34</sup>V. Deinhart, L.-M. Kern, J. N. Kirchof, S. Juergensen, J. Sturm, E. Krauss, T. Feichtner, S. Kovalchuk, M. Schneider, D. Engel *et al.*, *Beilstein J. Nanotechnol.* **12**, 304 (2021).
- <sup>35</sup>V. L. Mironov, B. A. Gribkov, A. A. Fraerman, S. A. Gusev, S. N. Vdovichev, I. R. Karetnikova, I. M. Nefedov, and I. A. Shereshevsky, *J. Magn. Magn. Mater.* **312**, 153 (2007).
- <sup>36</sup>A. V. Ognev, A. G. Kolesnikov, Y. J. Kim, I. H. Cha, A. V. Sadovnikov, S. A. Nikitov, I. V. Soldatov, A. Talapatra, J. Mohanty, M. Mruzckiewicz *et al.*, *ACS Nano* **14**, 14960 (2020).
- <sup>37</sup>K. D. Stenning, X. Xiao, H. H. Holder, J. C. Gartside, A. Vanstone, O. W. Kennedy, R. F. Oulton, and W. R. Branford, *arXiv:2112.00697* (2021).
- <sup>38</sup>T. Dion, D. Arroo, K. Yamanoi, T. Kimura, J. Gartside, L. Cohen, H. Kurebayashi, and W. Branford, *Phys. Rev. B* **100**, 054433 (2019).
- <sup>39</sup>R. W. Damon and J. R. Eshbach, *J. Phys. Chem. Solids* **19**, 308 (1961).
- <sup>40</sup>A. Bansil, H. Lin, and T. Das, *Rev. Mod. Phys.* **88**, 021004 (2016).
- <sup>41</sup>Y. Zhao, Q. Song, S.-H. Yang, T. Su, W. Yuan, S. S. Parkin, J. Shi, and W. Han, *Sci. Rep.* **6**, 22890 (2016).
- <sup>42</sup>P. Bruno, *Phys. Rev. Lett.* **93**, 247202 (2004).
- <sup>43</sup>V. K. Dugaev, P. Bruno, B. Canals, and C. Lacroix, *Phys. Rev. B* **72**, 24456 (2005).
- <sup>44</sup>A. Vansteenkiste, J. Leliaert, M. Dvornik, M. Helsen, F. Garcia-Sanchez, and B. Van Waeyenberge, “The design and verification of MuMax3,” *AIP Adv.* **4**, 107133 (2014).
- <sup>45</sup>D. Kumar, P. Sabareesan, W. Wang, H. Fangohr, and A. Barman, *J. Appl. Phys.* **114**, 023910 (2013).
- <sup>46</sup>X. S. Wang and X. R. Wang, *J. Appl. Phys.* **129**, 151101 (2021).
- <sup>47</sup>T. Fukui, Y. Hatsugai, and H. Suzuki, *J. Phys. Soc. Jpn.* **74**, 1674 (2005).
- <sup>48</sup>C. Wang, H. Zhang, H. Yuan, J. Zhong, and C. Lu, *Front. Optoelectron.* **13**, 73 (2020).